Earth Science Informatics (2023) 16:2595–2613
https://doi.org/10.1007/s12145-023-01047-y

RESEARCH

Estimation of the desert dust balance and its relationship with environmental factors in the southern Baja California Peninsula

Enrique De Jesús Morales-Acuña[1,2] · Sergio Aguíñiga-García[2] · Rafael Cervantes-Duarte[2] · Jean Linero-Cueto[3]

Received: 21 February 2023 / Accepted: 3 July 2023 / Published online: 1 August 2023

Abstract

The emission, transport, and deposition of desert dust are influenced by environmental factors evaluated mainly as a function of precipitation, air temperature, and wind. The present study estimates the desert dust balance and its relationship with environmental factors for the period 1981–2020 in the Baja California Sur region, Mexico. Monthly data on wind, air temperature, precipitation, dust emission and deposition from in situ measurements, reanalysis, satellite estimates and a numerical parameterization scheme are used. First, the in-situ time series were reconstructed with a non-linear principal component analysis based on an autoassociative neural network. We then evaluated the performance of the satellite estimates and the reanalysis data using the matching technique, after which we quantified the dust emission in three source zones. To estimate the state of the climate, we obtained the annual cycle of monthly climatologies, and yearly averages. The effect of climate on the dust budget is estimated by means of non-parametric associations between the variables of interest. Finally, we estimate climate trends using Pettitt, Modified Man-Kendall and Theil-Sen tests. The results show that the data sets used represent the mean and variability of in situ measurements. There are three seasons with transitional periods for precipitation and air temperature. The wind shows a longitudinal west–east gradient. Its maximum intensity is from April to September. Northern zone was dominated by highest emissions. Dry deposition mechanism was the most representative. Emissions and dry deposition are controlled by wind intensity and precipitation, while precipitation controls wet deposition. The Pettitt test showed that abrupt changes in the time series coincide with periods where positive sunspot anomalies converge with negative PDO and SOI anomalies. Finally, trend analyses identified a temporal broadening of the dry season, warmer winters, and summers with increases of ~ 0.02 °C, predominantly increasing trends in dust emissions and wind intensity, and a progressive decrease in dust deposition mechanisms.

Keywords Climate variability · Trends Analysis · Mann–Kendall Test · Pettit Test · Dust Emission

Introduction

The analysis of climatic conditions in different regions of the world has been established mainly in terms of air temperature, precipitation, and wind (e.g., Aliaga et al. 2017; Almazroui et al. 2020; Jardim et al. 2021). Consequently, the Intergovernmental Panel on Climate Change (IPCC) estimates, in its different scenarios, increases in the probability of adverse events such as droughts, forest fires, intensification of tropical cyclones, and floods (IPCC 2014). These increases are mainly reflected in gradual increases in mean annual air temperature and precipitation by the end of the

Communicated by H. Babaie.

✉ Jean Linero-Cueto
jlineroc@unimagdalena.edu.co

Enrique De Jesús Morales-Acuña
emoralesacu1980@gmail.com

Sergio Aguíñiga-García
saguini@ipn.mx

Rafael Cervantes-Duarte
rcervan@ipn.mx

[1] Centro Interdisciplinario de Investigación Para El Desarrollo Integral Regional, Instituto Politécnico Nacional, Bulevar Juan de Dios Bátiz Paredes #250, Col. San Joachin, en Guasave, Sinaloa, México

[2] Centro Interdisciplinario de Ciencias Marinas, Instituto Politécnico Nacional, Av. IPN, Playa Palo de Santa Rita, La Paz, B.C.S, México

[3] Facultad de Ingeniería, Universidad del Magdalena, Carrera 32 No. 22-08, 470004 Santa Marta, Magdalena, Colombia

twentieth century (IPCC 2015). Proof of this is the increasing trends of rainfall that have recently been reported in some regions of the world such as Central Africa (Almazroui et al. 2020), the northwestern United States with 3% increases in rainfall's extremes (Nazarian et al. 2022), and South America (southern Brazil, Uruguay and northeastern Argentina), where the main contributors are natural climate variability, variations in the composition of the atmosphere, and radiative forcing associated with anthropogenic activities (de Barros et al. 2016).

One of the elements resulting from natural and anthropogenic processes, which influence the climate system, is the dust concentration emitted from deserts. These impact the Earth's energy balance through interactions with radiation, clouds, atmospheric chemistry, cryosphere, and biogeochemistry (Kok et al. 2022). For mineral dust particles to reach impact in this way they must complete a cycle, this one divided into three phases: emission, transport, and deposition (Shao et al. 2011). Emission is the result of wind interaction with the earth's surface. While transport depends exclusively on particle size, anthropogenic activities (such as land use change), and wind intensity. Deposition, on the other hand, is established by two mechanisms: dry and wet deposition, which are mainly associated with fluctuations in wind intensity and rainfall, respectively (Bergametti & Forêt, 2014).

Once desert dust is deposited to the ocean could influence on marine primary productivity (Mahowald et al. 2014; Muñoz-Barbosa et al. 2020; Wang et al. 2017), and cause cooling at the ocean Surface (Evan et al. 2009; Martínez Avellaneda 2010; Safaierad et al. 2020). Examples of this are the effects of Saharan intrusions in the Caribbean Sea and the Gulf of Mexico, reported by Martínez Avellaneda (2010). Studies on desert dust trends indicate increases in dust emission from different regions of the world that are congruent with variations in precipitation, base soil and surface wind speed projected by IPCC (Ji et al. 2018; Okin & Reheis 2002; Pu & Ginoux 2017).

The northwestern region of Mexico has a big land extension surrounded by the Gulf of California and the Pacific Ocean. It is divided in two states: Baja California and Baja California Sur. The last one has been characterized as a relevant source of desert dust (Morales-Acuña et al. 2019b), and due to its climatic characteristics, land use and management, it is vulnerable to the effects of climate change, as evidenced by the intensification of desertification processes (Salinas-Zavala et al. 2017; SEMARNAT 2016; Troyo-Diéguez et al. 2014), rainfall decrease (Colorado-Ruiz & Cavazos 2021; Morales-Acuña et al. 2019b), and air temperature raising (Colorado-Ruiz & Cavazos 2021; Martínez-Austria & Jano-Pérez 2021).

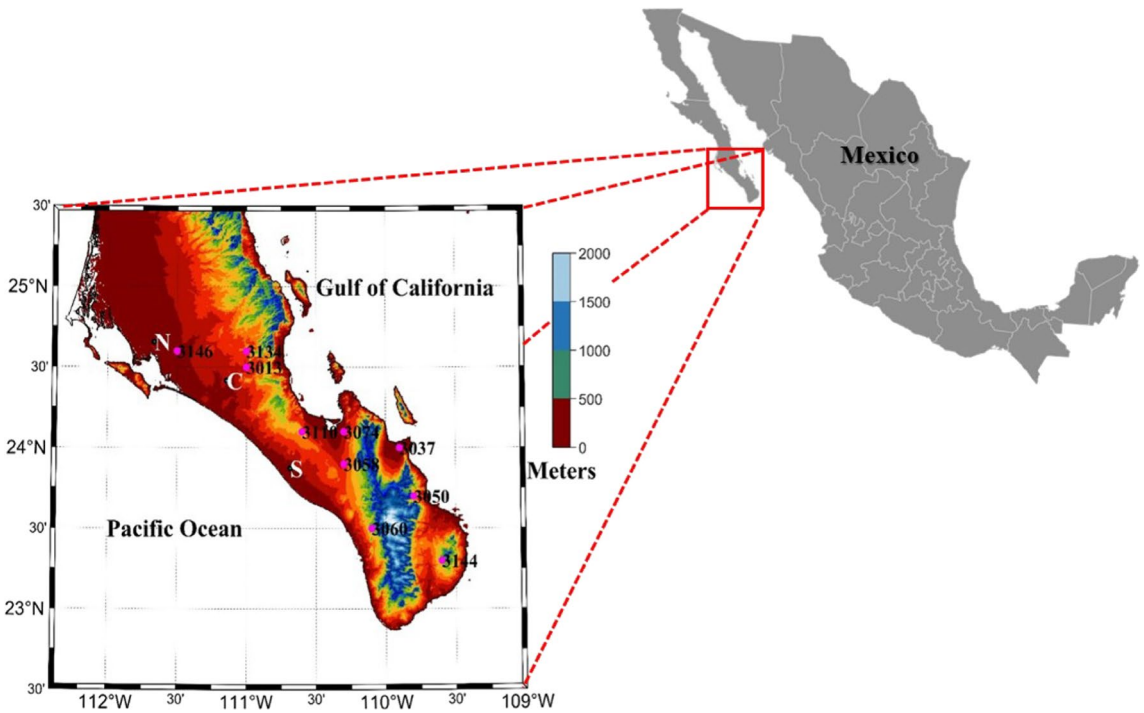

Fig. 1 Study area. The orography of the region is shown in color. The depths are shown in black outlines. In magenta circles, the location of CLICOM weather stations with their respective codes. N, C, and S are the North, Central, and South regions that act as dust sources, according to Martínez-Flores et al. (2013)

These scenarios allow inferring that the desert dust inventory in this region could be increasing, driving impacts on public health, aquatic ecosystems, and climate. For this reason, this work seeks to estimate the climate trends in Baja California Sur and its association with the inventory of desert dust (from January 1981 to December 2020) emitted from point sources distributed in this region.

Data and methods

Study area

The southern region of the Baja California Peninsula (RSBCP) (Fig. 1), located between 22°- 24° N and 115°—109° W, has a mountain range with a maximum elevation of 2160 m and is surrounded by the Pacific Ocean to the east and the Gulf of California to the west (Fig. 1). The pluviometric regime for this region establishes two subregions whose differences are framed by the presence of the Sierras and the plains of the region, such that the maximum average annual rainfall is found in the south (310 mm year^{-1}) and the minimum in the north (120 mm year^{-1}) (Salinas-Zavala et al. 1990; Troyo-Diéguez et al. 2014). The mean annual pattern is distributed in three seasons; two rainy seasons (July–October, November-February) and one dry season (March-June) (Salinas-Zavala et al. 1990).

The RSBCP during the summer the temperature can exceed 40 °C, while in the winter, it oscillates between 5 and 12 °C, excluding the Sierra de la Laguna region (Troyo-Diéguez et al. 2014). The wind pattern during the summer establishes predominantly westerly direction with intensities < 3 m s^{-1} (Morales-Acuña et al. 2019a, b); in the other climatic seasons, the wind direction obeys the Pacific wind pattern (Morales-Acuña et al. 2019b).

The arid and semi-arid characteristics of the region allow the identification of extensive areas that Martínez-Flores et al. (2013) classified as a dust source, located mainly to the north of this region, and distributed southward along the coastal area adjacent to the Pacific Ocean. Regarding the predominant vegetation, 83% of the vegetation cover in this region consists of tropical dry forest and xerophytic scrub. Additionally, the zonal vegetation in coastal areas corresponds to sclerophyllous chaparral and succulent scrub along the Thermo-Mediterranean and Inframediterranean belts, respectively, and to different types of thermo-tropical-desert vegetation in the rest of the peninsula (Peinado et al. 2008). In this region of Mexico, it has been determined that the most predominant soil types are Regosol (39.99%) and Leptosol (29.71%). In addition, Arenosol participates in this classification with 2.12% (INEGI 2010).

Description of databases

Land-based rainfall and air temperature measurements

Daily mean precipitation and air temperature data for the period 1981 to 2015 from 10 weather stations distributed as shown in Fig. 1 were obtained from the CLImate COMputing (CLICOM) project available at http://clicom-mex.cicese.mx/. CLICOM, a climatological data management software system developed by the United Nations, uses a database of surface weather stations from the National Meteorological System of Mexico (S.M.N, 2023), which also performs quality control of the information provided in their data portals. The location of the weather stations used in this study is shown in Table 1.

Satellite measurements

CHIRPS (Climate Hazards Group InfraRed Rainfall with Station data) is an estimated rainfall database created and managed by the U.S. Geological Survey (USGS) and the University of California, Santa Barbara (UCSB). The information is distributed in NetCDF4 format with different temporal resolutions, from daily to decades. The spatial resolution of these data is 0.05°. CHIRPS are based on data from the Climate Hazards Rainfall Climatology—(CHPClim), Geostationary Thermal Infrared (IR) sensor, Tropical Rainfall Measuring Mission (TRMM) satellite mission, NOAA Climate Forecast System (CFSv2) atmospheric rainfall field model, and in situ rainfall observations from various sources including U.S. and regional meteorological services (Funk et al. 2015).

Reanalysis products

Monthly data (1981–2020) at 0.1° resolution for the zonal and meridional wind components, and air temperature, were obtained from ERA5-Land (https://cds.climate.coper

Table 1 Location of CLICOM weather stations

Code	Station	Longitude	Latitude	Altitude
3013	El Pilar	-111	24.5	120
3037	San Juan De Los Planes	-109.9	24	20
3050	San Bartolo	-109.8	23.7	395
3058	San Pedro	-110.3	23.9	190
3060	Santa Gertrudis	-110.1	23.5	520
3074	La Paz	-110.3	24.1	16
3110	Alfredo V. Bonfil	-110.6	24.1	70
3134	Los Cantilitos	-111	24.6	160
3144	Mangle	-109.6	23.3	285
3146	Santa Rita	-111.5	24.6	45

nicus.eu). ERA5-Land is a reanalysis data set that provides a consistent view of the evolution of ground-based variables over several decades with improved resolution compared to ERA5. ERA5-Land has been produced by reproducing the ground-based component of the ECMWF ERA5 climate reanalysis. The reanalysis combines model data with observations from around the world into a globally consistent and complete data set.

The approximate monthly time series of area-averaged dry and wet dust deposition for the marine region of the La Paz Bay (LPB) for the period 2003–2020 were obtained from https://giovanni.gsfc.nasa.gov/; these global data are the product of a MERRA-2 model with a 0.5 × 0.6° of spatial resolution.

Methods

Pre-processing of databases

An algorithm developed in the MATLAB R2022a programming language was used to search for missing data in the time series obtained from the CLICOM database. The series with missing data were reconstructed using a Non Linear Principal Component Analysis (NLPCA) with inverse network architecture and a total of 3000 iterations based on an autoassociative neural network proposed by Scholz et al. (2008). This technique is available at http://www.nlpca.org/matlab.htm and has been successfully used in the reconstruction of hydrological time series (Canchala et al. 2020; Miró et al. 2017). In this study, standardized spatial anomalies were initially calculated; subsequently, the NLPCA analysis was applied, obtaining reconstructed spatial anomaly series for each analyzed variable. Finally, the reconstructed series were obtained by multiplying the reconstructed standardized spatial anomaly series by the standard deviation of the original data, and the arithmetic mean of these was summed, as shown in Eq. 1.

$$S_{rc} = \left(x_{rc} \times \delta_i\right) + \overline{x_i} \tag{1}$$

where S_{rc} is the reconstructed series, x_{rc} is the reconstructed standardized spatial anomaly series. δ_i y $\overline{x_i}$, are the standard deviation and mean of the in situ data provided by CLICOM, respectively. To evaluate the model performance and forecasting ability at both training and test time stamps, we used two statistical methods: root means square error (RMSE) and Spearman correlation coefficients ($r_{Spearman}$), applying Eqs. (2) - (3), respectively.

$$\mathrm{RMSE} = \sqrt{\frac{\sum_{i=1}^{n}\left(\mathrm{S}_i - \mathrm{S}_{\mathrm{rc}i}\right)^2}{n}} \tag{2}$$

$$r_{Spearman} = \frac{\sum_{i=1}^{n}\left\{\left(\mathrm{S}_{\mathrm{rc}i} - \overline{\mathrm{S}_{\mathrm{rc}}}\right)\left(\mathrm{S}_i - \overline{S}\right)\right\}}{\sqrt{\sum_{i=1}^{n}\left(\mathrm{S}_{\mathrm{rc}i} - \overline{\mathrm{S}_{\mathrm{rc}}}\right)^2}\sqrt{\sum_{i=1}^{n}\left(\mathrm{S}_i - \overline{S}\right)^2}} \tag{3}$$

where S_i and $S_{rc\,i}$ are the range of the measurement taken on the i-th element of the series, $\overline{S}$ y $\overline{S_{rc}}$ represent the average ranges, respectively.

The data from the different sources (reanalysis and satellite) were spatially trimmed, considering the RSBCP location, and the matching pixels with this region. So that a set of geospatial information was obtained and concatenated into three-dimensional matrices: longitude, latitude coordinates, and time. After selecting matching pixels with the study area, the erroneous data in the matrices were replaced by non-existent data (NaN). With the classified monthly arrays, multiyear series were obtained. For each variable, maps of the multi-annual monthly cycle and the annual mean were presented to visualize each variable's spatial distribution in the RSBCP. Climatology of cumulative monthly rainfall and total annual rainfall for 1981–2020 was obtained.

Rainfall and air temperature data validation

The evaluation of CHIRPS and ERA5-Land products was carried out from 1981 to 2015, using data from 10 weather stations located at different points in the RSBCP. First, grid values of rainfall and air temperature estimates for each rainfall station coordinate were extracted. Subsequently, comparative metrics were evaluated (Table 2). Within the comparative metrics, Spearman's correlation coefficient (ρ), mean absolute error (MAE), and bias (B) were considered (See, for example, Alemu & Bawoke 2019; Dinku et al. 2018; Urrea et al. 2016).

D is the difference between two samples ranges, and N is the number of ranges. C_i is the amount of rainfall or air temperature derived from weather stations. S_i represents the satellite-derived rainfall estimate or ERA5-Land air temperature, as appropriate. n is the total number of data.

Quantification of dust emission

The numerical parameterization scheme for dust emission E $\left(\mathrm{mgm^{-2}s^{-1}}\right)$ as a function of soil characteristics and grain size

Table 2 Comparison metrics were used to evaluate monthly air temperature and rainfall data from CHIRPS and ERA5-Land for 1981–2020

Statistic	Formula	Range	Units
Spearman Correlation Coefficient	$\rho = 1 - \frac{6\sum D^2}{N\left(N^2-1\right)}$	-1 a 1	none
Absolute Mean Error	$MAE = \frac{1}{n}\sum_{i=1}^{n}\left\|S_i - C_i\right\|$	0 a ∞	mm, °C
Bias	$B = \frac{\sum_{i=1}^{n} S_i}{\sum_{i=1}^{n} C_i}$	0 a ∞	none

distribution (Eq. 4), proposed by Shao et al. (1993), modified by Nickovic et al. (2001) and adjusted for Baja California Peninsula by Morales-Acuña et al. (2019b), will be used to calculate dust emission from three locations acting as uniformly distributed dust sources as shown in Table 3.

$$E = C\delta \mathbf{u}_*^3 \left[1 - \left(\frac{\mathbf{u}_*^t}{\mathbf{u}_*}\right)^2\right] \tag{4}$$

where $C(\mathrm{mgm^{-5}s^2})$ is an empirical dimensional constant ($C = 1.7195\mathrm{mgm^{-5}s^2}$, Morales-Acuña et al. 2019b). $\mathbf{u}_*^t$ and $\mathbf{u}_*$ $(\mathrm{ms^{-1}})$ are the frictional threshold velocity ($\mathbf{u}_*^t = 0.25\mathrm{ms^{-1}}$ Ginoux 2017; Ginoux et al. 2012; Nickling & Gillies 1993; Westphal et al. 1987) and the wind friction velocity which was calculated for conditions of unstable atmospheric stability as proposed by Morales-Acuña et al. (2019b).δ is a dimensionless factor referring to dust productivity (Eq. 5) that depends on vegetation, the fraction of the area susceptible to erosion and types of soil, and the relative contribution of each of these factors.

$$\delta = \alpha\gamma_k\beta_k \tag{5}$$

where α is the vegetation factor defined as:

$$\alpha^{i,j} = \frac{\sum_{n=1}^{N} M_n^{i,j}}{N} \tag{6}$$

M is the mask of the desert as a function of vegetation, and N is the number of pixels in the grid of the mask. In the present work $\alpha = 1$ (Nickovic et al. 2001), because our study area is represented as a single pixel for each point source; vegetation can be neglected because this area has been considered to be sand desert with scarce vegetation (Morales-Acuña, 2015). Tegen & Fung (1994) assume an erodible fraction γ_k (Eq. 5) as a function of particle type. In our calculations we specify $\gamma_k = 0.17$. The soil factor and relative contribution β_k (Eq. 5) will be considered according to the predominant granulometry in the study areas and to the particle size whose time-life in the atmosphere facilitates long-distance transport, i.e., the relative contribution of sands and clays, so that $\beta_k = 0.25$ (Table 2. Nickovic et al. 2001). After calculating each value in Eq. 5, the dust productivity factor in this work is set as $\delta = 0.0425$.

Table 3 Geographic distribution of dust source areas located in the RSBCP

Zone	Longitude	Latitude
North (N)	-111.666187	24.657002
Center (C)	-111.144705	24.417142
South (S)	-110.685795	23.87328

Associations of dust emissions with hydrometeorological variables

Once the monthly arrays of each of the hydrometeorological variables were obtained, the nearest neighbor technique was applied to extract from each matrix the monthly time series of the matching pixel with the geographic location of the dust source area in which the emission was calculated. Subsequently, statistical associations were made with Spearman's coefficient as shown in the following section.

Temporary trends

The nature of time series can have abrupt changes or breaks in which the behavior can change to increase or decrease from this. Considering the above, the different variables analyzed in this study will be evaluated using Pettitt's test (Pettitt 1979). This test approximates a sequence of random variables belonging to non-parametric methods. It is used to identify a change point in a time series and can be described as follows: Once the breakpoint of a time series is detected, the data set is divided into two intervals by classifying the samples coming from the same population into before $(x_1, x_2, \ldots x_t)$ and after $(x_{t+1}, x_{t+2}, \ldots x_T)$ the breaking point. The $U_{t,T}$ test statistic is given by (Eq. 7):

$$U_{t,T} = \sum_{i=1}^{t} \sum_{j=t+1}^{T} sgn(x_t - x_j) \tag{7}$$

The most significant change point is obtained when $K_T = \max|U_{t,T}|$, the significance level is determined in our work for $\rho < 0.05$, in such a case the null hypothesis is rejected, this value is calculated by the expression $\rho = \exp\left(\frac{-6K_T^2}{T^3+T^2}\right)$. If there is a significant change point, the time series is divided into two parts at the location of the change point.

Once the change points of the time series have been obtained, the trend of the time series of the different variables will be evaluated. First, the Modified Mann–Kendall non-parametric test proposed by Hamed & Rao (1998) was applied for each pixel of the matrix belonging to the study area. The Mann–Kendall test obtains the S-statistic (Eq. 8), considering the length n of a time series data and the elements x_i y x_j a time interval i y j.

$$S = \sum_{i=1}^{n-1} \sum_{j=i+1}^{n} sgn(x_j - x_i) \tag{8}$$

where,

$$sgn(x_j - x_i) = \begin{cases} 1 for (x_j - x_i) > 0 \\ 0 for (x_j - x_i) = 0 \\ -1 for (x_j - x_i) < 0 \end{cases}$$

If the data are identical and have an independent distribution, with a mean value of S equal to zero, the variance will be given by (Eq. 9):

$$V(S) = \frac{n(n-1)(2n+S)}{18} \tag{9}$$

The statistical value of the Mann–Kendall test is obtained by the following expression:

The hypothesis test is with H0 indicating no trend in the time series while H1 indicates a trend. H0 is rejected with a confidence level of 95% if $|z| > 1.96$. Suppose the coefficients resulting from this test have autocorrelation. In that case, the trend values may be over or underestimated (Hamed & Rao 1998), so the modified Mann Kendall test considers the structure of the significant autocorrelation coefficients in the time series data. This is achieved by modifying the variance V used to calculate the z-value of the original Mann–Kendall method such that:

$$V(S)^* = V(S)\frac{n}{n^*} \tag{10}$$

$$\frac{n}{n^*} = 1 + \frac{2}{n(n-1)(n-2)} \sum_{n=1}^{n-1} (n-i)(n-i-1)(n-i-2)r_i \tag{11}$$

where r_i is the significant autocorrelation coefficient at the i-th order of the data and n^* is represented as an effective number of observations to account for the autocorrelation in the data. Sen's slope estimator was used to calculate the actual slope of trends in cumulative rainfall time series data. If a linear trend exists, the magnitude of the monotonic trend in hydrologic time series can be quantified using Sen (1968) nonparametric slope estimator using Eq. 12.

$$\beta = median\left(\frac{x_j - x_i}{j-i}\right) \tag{12}$$

β represents the slope mean values between data measurements x_j and x_i at time steps *jei* con $j > i$, respectively. The positive value of β indicates an increasing trend while the negative value of β indicates a decreasing trend. The sign of β reflects the direction of the trend of the data, while its value indicates the slope of the trend. The advantage of this method is that it limits the influence of missing values or outliers on the slope compared to linear regression.

Results

Reconstruction and validation of databases

The quality control for the CLICOM time series identified that only the air temperature series had discontinuities. These were reconstructed at 95% confidence level, a correlation coefficient of 0.92, and a mean square error of 4.6×10^{-5}, on average for ten selected stations.

For precipitation, the validation metrics allowed us to identify (with a 95% confidence level) that the CHIRPS-v2.0 data slightly underestimate the rainfall values from the weather stations, with a mean bias of 0.95 (Fig. 2a). This behavior is mainly observed at the La Paz station. On the other hand, the monthly variability of the CHIRPS-v2.0 data adequately represents that of the rain gauges, such that Spearman's correlation coefficient has a mean value of 0.8.

Comparisons between the ERA5-Land air temperature databases with those provided by CLICOM (Fig. 3) identified an average correlation above 0.9 (95% confidence) and an average bias of 1.005. At two stations, the ERA5-Land temperature values slightly overestimate those in situ stations. The average MAE obtained (1.54 °C) shows that the absolute difference between the two measurements leads to minor errors.

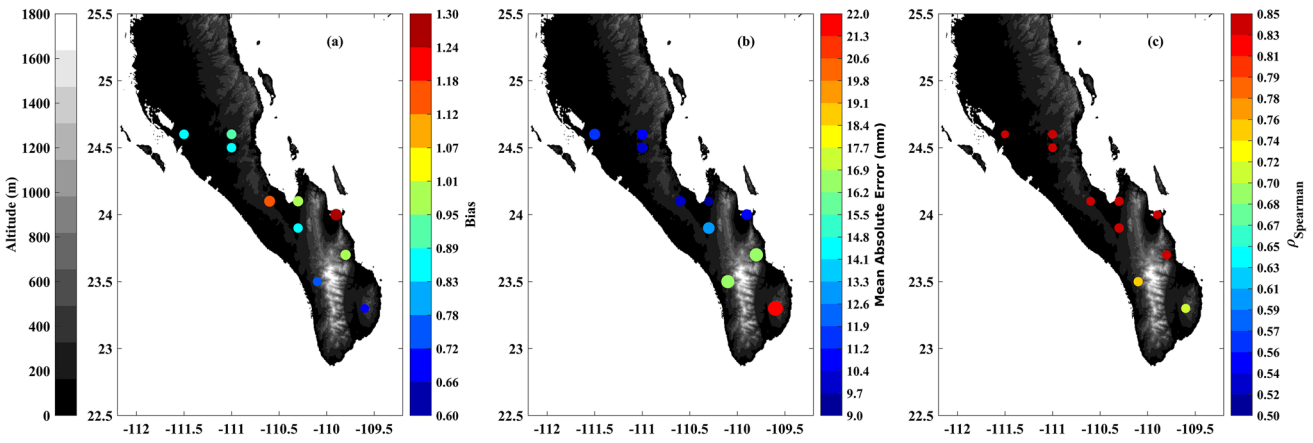

Fig. 2 Comparative metrics between CHIRPS data and CLICOM weather stations. In gray scale the topography of the region is shown, and in color scale (**a**) Bias, (**b**) Mean Absolute Error, and (**c**) Spearman Correlation Coefficient for the period 1981–2015

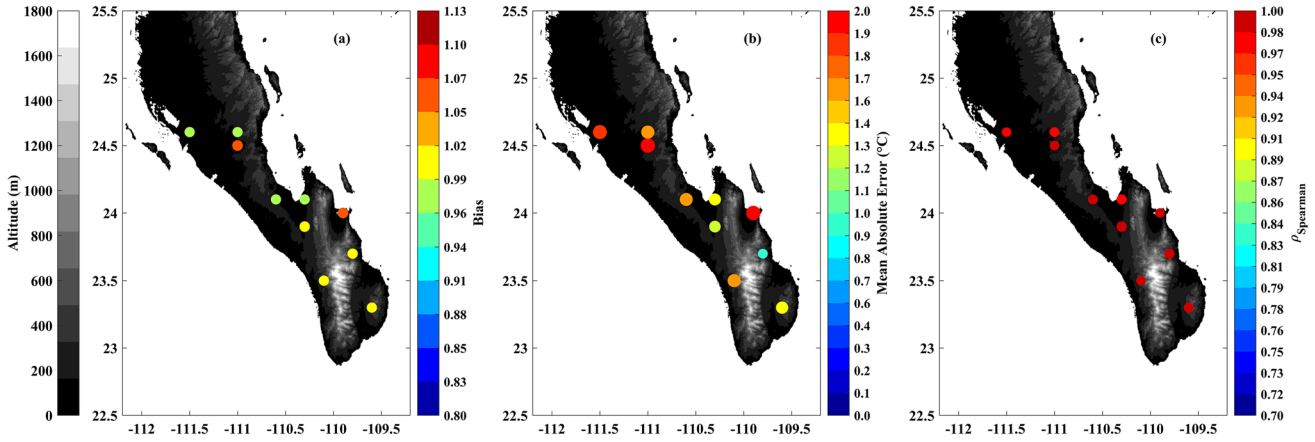

Fig. 3 Comparative metrics between ERA5-Land and CLICOM air temperature data: In grayscale, the topography of the region is shown and in color scale (**a**) Bias, (**b**) Mean Absolute Error and (**c**) Spearman's Correlation Coefficient (1981–2015)

Climatology of the hydrometeorological variables

The climatology of the accumulated monthly rainfall (Fig. 4) allowed us to identify the existence of two rainy seasons, one dry season and two transition months explained below: (1) High rainfall (> 110 mm month^{-1}), comprised from July to September, (2) low rainfall (50—100 mm month^{-1}), during December and January, (3) Dry, with rainfall less than 50 mm month^{-1} from March to June. February and October are transition months between one season and the other. On the other hand, total annual rainfall presented maximum values in the south (> 300 mm month^{-1}) and minimum values (< 200 mm month^{-1}) in the center and north of the region.

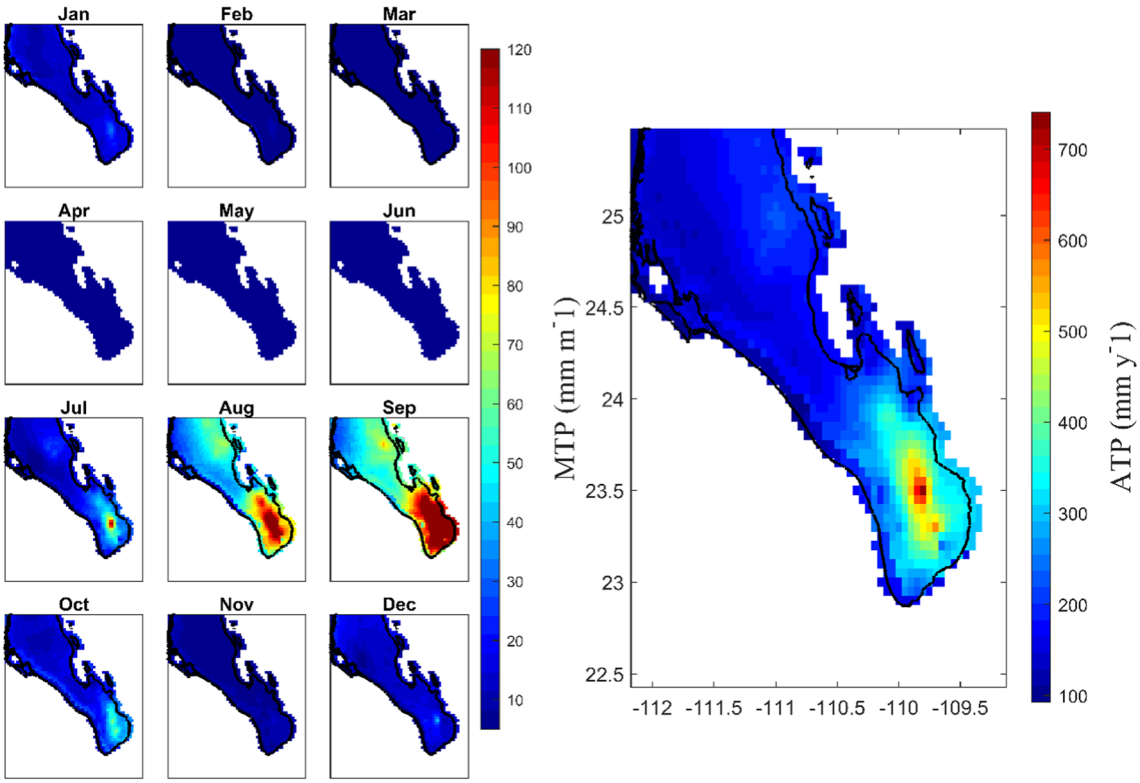

Fig. 4 Climatology of cumulative monthly rainfall (left panel) and total annual rainfall (right panel) for 1981–2020

The monthly climatology of air temperature (Fig. 5) identified July–September as the months with the highest temperatures (> 28 °C), excluding the highland region located in the south of the study area. The lowest temperatures (< 20 °C) occurred during December-March. From April to June, temperatures are in the range 22—27 °C. November seems to be a transition month.

The mean annual temperature in the study area presents a west–east longitudinal gradient with lower temperatures (< 21 °C) in the southern and northeastern regions. The highest temperatures (> 24 °C) occurred in the coastal region adjacent to the CG.

The analysis of the wind fields for the annual cycle (Fig. 6) established a longitudinal gradient in wind intensity, with higher intensities (> 3 ms^{-1}) on the Pacific Ocean coasts and lower intensities (< 1.5 ms^{-1}) in the coastal region of the GC. On the other hand, it is observed (Fig. 6) that in the areas of high topography, the wind intensity has lower values concerning the plains regions. The predominance of maximum values for wind intensity occurs from April to September, being the June–August quarter the one with the highest intensities.

From April to September, the predominant wind direction is from the west, with a characteristic behavior in which the air masses that encounter the mountain massif will re-direct themselves taking a northeasterly direction and, in some cases, bordering the mountain. From November to February, the predominant wind is from the north, while October, March, and May, the predominant direction is from the northwest. The mean annual wind field (Fig. 6, left panel) allows us to identify a predominant direction from the northwest and intensities of 1 to 4 ms^{-1} distributed spatially along a longitudinal west–east gradient. To the south of the study region, the lowest intensities are found just in the mountain zone.

Desert dust budget

The monthly dust climatology emitted from the three source regions in the (Fig. 7) allow identifying a unimodal behavior with maxima in May and minima in December, January, and November, for the North, Central, and South region, respectively. Dust emission rates from these three regions ranged from 0.54 y 466.42 $mgm^{-2}s^{-1}$. The Northern region was dominated by higher values (> 350 $mgm^{-2}s^{-1}$), while the Central region was dominated by lower values (< 50 $mgm^{-2}s^{-1}$). The boxplot diagrams show that the highest dispersion of the data is had during summer, and the lowest is observed in winter.

The mechanisms of desert dust deposition on LPB during the period 2003–2020 (Fig. 8) allowed use to establish that dry deposition has the maximum values concerning

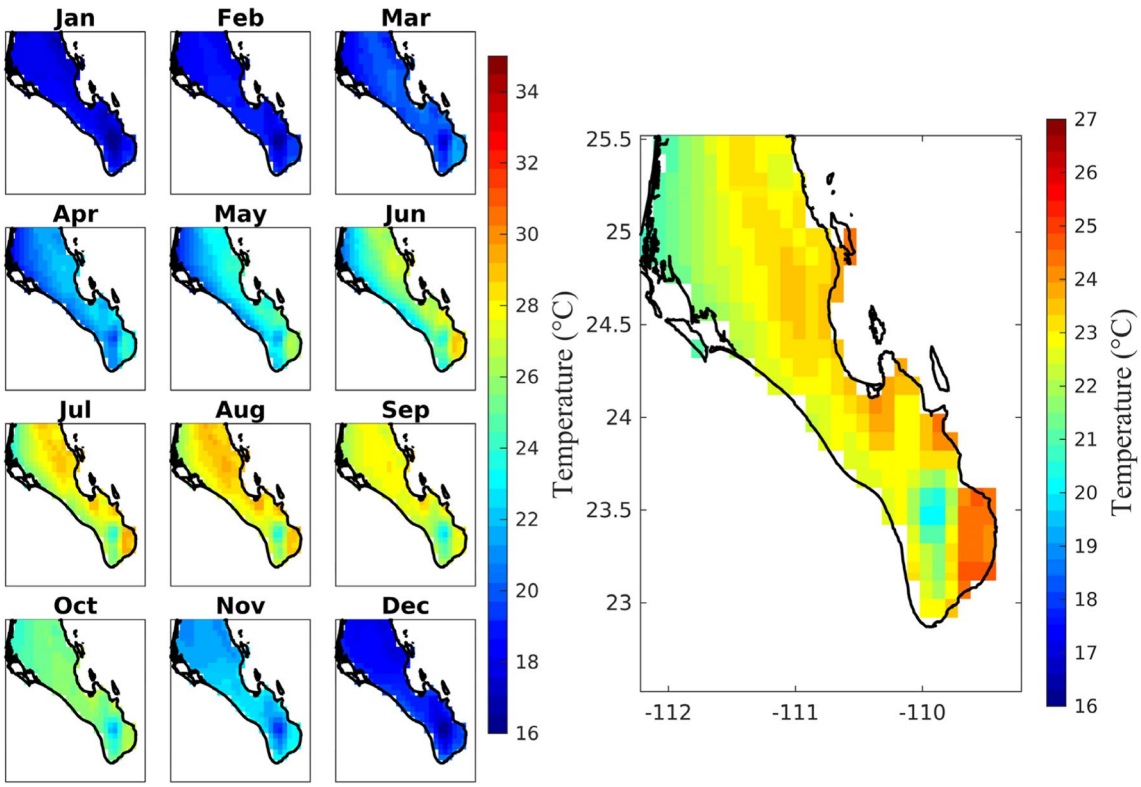

Fig. 5 Climatology of monthly air temperature (left panel) and annual mean temperature (right panel) for 1981–2020

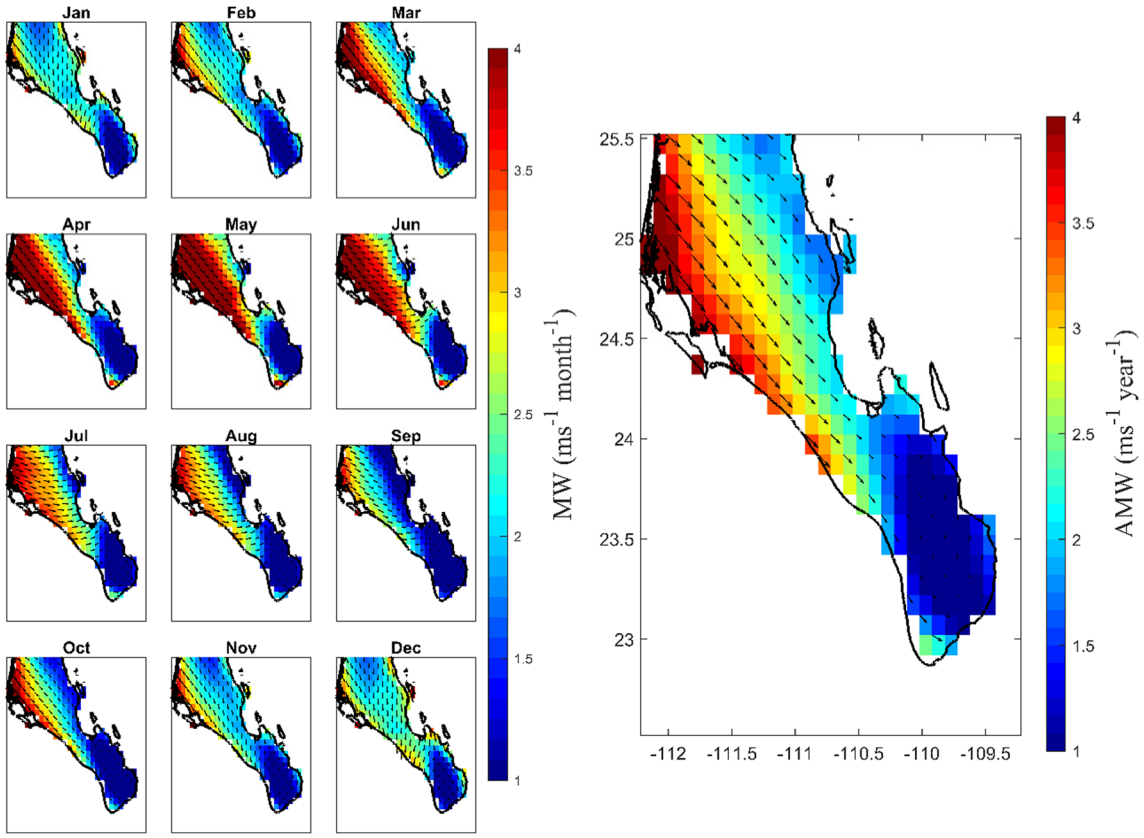

Fig. 6 Climatology of mean wind fields (left panel) and annual mean-field (right panel) from 1981–2020

wet deposition in such a way that it exceeds an average of 0.1661 $mgm^{-2}s^{-1}$ to wet deposition. Referring to the annual cycle of the monthly climatology of dry deposition (Fig. 8), a unimodal behavior can be observed whose maxima seem to be associated with the seasons of maximum dust emission obtained in the three studied localities. The

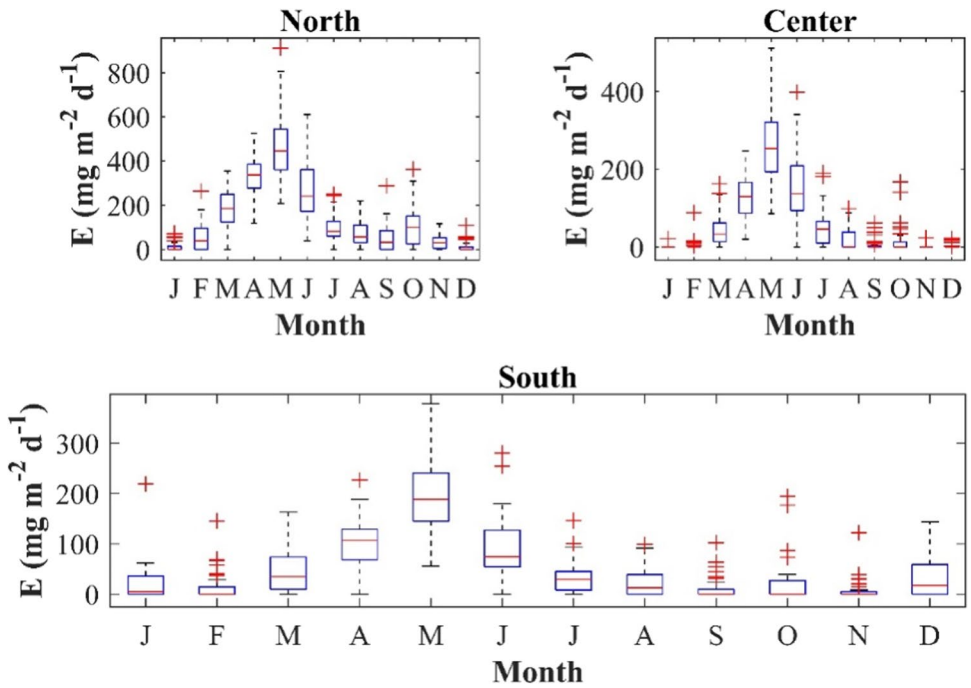

Fig. 7 Monthly climatologies of desert dust emission from three zones of the RSPBC (1981–2020)

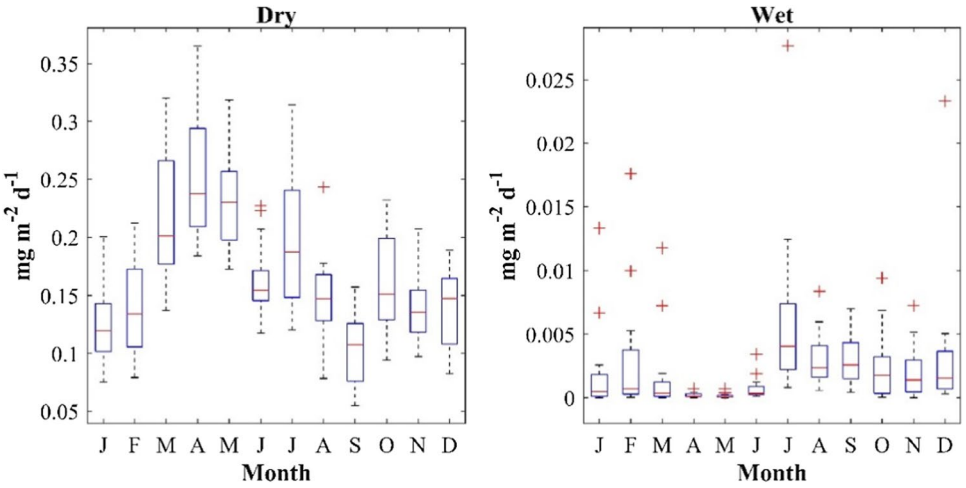

Fig. 8 Climatology of desert dust deposition over La Paz Bay during 2003–2020

minimum (0.10 $mgm^{-2}s^{-1}$) and maximum (0.25 $mgm^{-2}s^{-1}$) values for dry deposition occurred in the months of September and April, respectively.

On the other hand, the wet deposition of desert dust in the LPB (Fig. 8) allowed identifying a unimodal behavior with maxima during the July to October seasons; this season is associated with the arrival of tropical cyclones with heavy rainfall as reported by Cavazos et al. (2008). Therefore, the minimum (0.0001 $mgm^{-2}day^{-1}$) and maximum (0.006 $mgm^{-2}day^{-1}$), values for this desert dust deposition mechanism are established in May and July, respectively.

Associations of desert dust with air temperature, wind, and rainfall

The leading associations between air temperature (at 2 m) and rainfall were found in the northern region and the minimum associations in the central region (Table 4). In addition, it can be observed that dust emission is directly associated with wind and inversely with rainfall. Air temperature presented low associations; for the case of the northern region, the associations were not statistically significant.

The dry deposition mechanism was directly related to wind and inversely related to rainfall, while wet deposition was inversely related to wind, with rainfall dominating. Air temperature presented statistically significant associations only with the wet deposition mechanism (Table 5).

Temporal trends of air temperature, rainfall, and desert dust budget

After evaluating the breakpoints in each rainfall time series, monthly air temperature, wind, and dust emission at 95% confidence level, we found the year 2000 as this breakpoint in all these variables. Both dry and wet deposition mechanisms, the breaking point was 2011.

The trends for the annual rainfall cycle (Figs. 9 and 10) allow identifying a decreasing behavior with values between 0.05 and 0.3 $mmyear^{-1}$ (at 95% confidence level). The high rainfall season contains the most significant decreases, with September being the most representative month in this behavior. On the other hand, the low rainfall season shows an average decrease of 0.2 $mmyear^{-1}$ in almost every region.

Months with the most significant temperature increases in almost the entire region were March and November, with the former showing the highest trends (> 0.025 °C $year^{-1}$). A characteristic feature is during the months with lower temperature values, the trends are positive (Fig. 5, December-March). The same behavior occurs during the summer months (Fig. 5, June–August).

Table 4 Associations of dust emission with rainfall, air temperature, and wind intensity in three RSBCP dust source regions during 1981–2020. N = 480 and 95% confidence. Statistically significant values are highlighted in bold

	Rainfall	Temperature	Wind
North	**-0.729**	-0.022	**0.996**
Center	**-0.563**	**0.182**	**0.945**
South	**-0.567**	**-0.164**	**0.982**

Table 5 Associations between dust deposition mechanisms (dry and wet) and rainfall, air temperature, and wind intensity from 2003–2020. With an N = 216 at 95% confidence level. Statistically significant values are highlighted in bold

Depositation	Rainfall	Temperature	Wind
Dry	**-0.52**	-0.06	**0.58**
Wet	**0.58**	**0.21**	**-0.25**

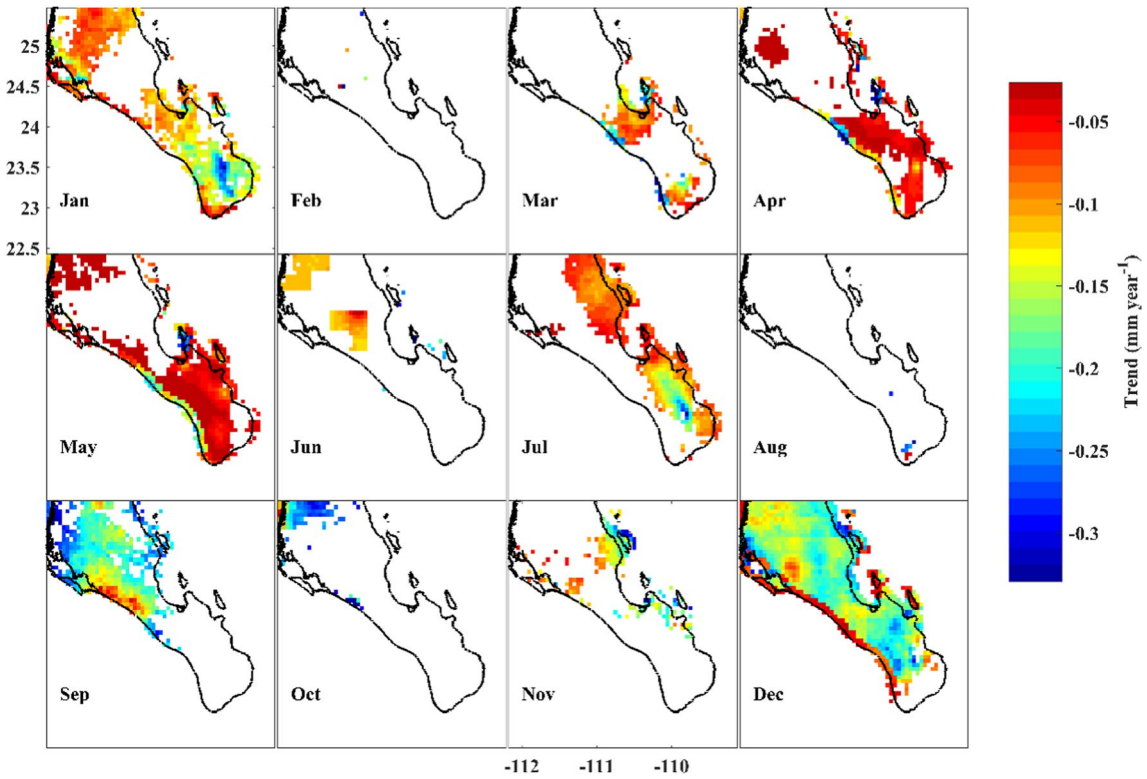

Fig. 9 Temporal trends for the annual rainfall cycle during the period 1981–2020, at 95% confidence level

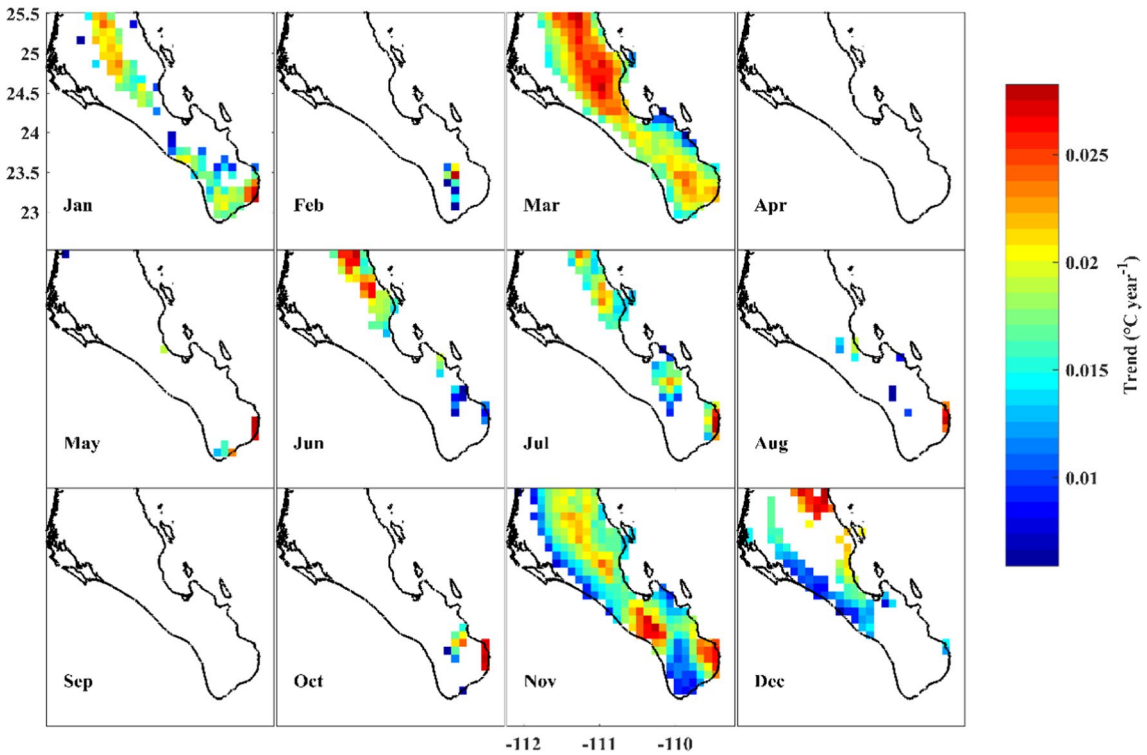

Fig. 10 Temporal trends of the annual air temperature cycle for 1981–2020, at 95% confidence level

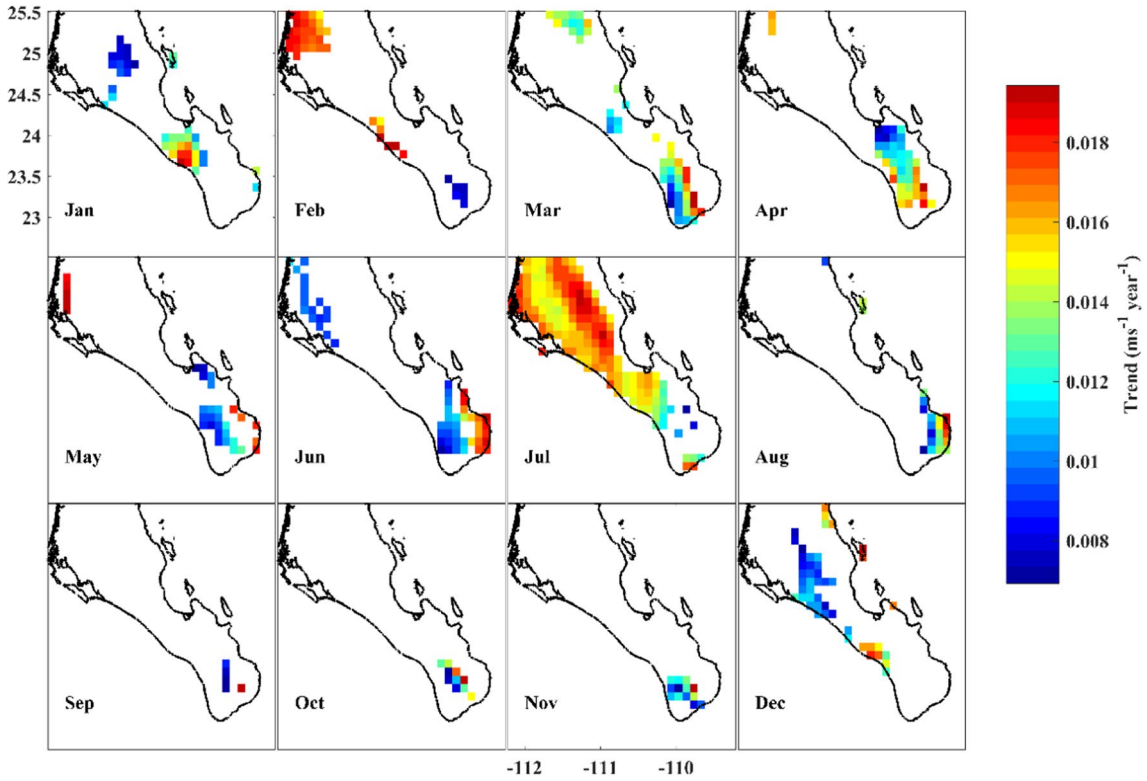

Fig. 11 Temporal trends of the annual cycle of wind intensity for 1981–2020, at 95% confidence level

The trend analysis for the annual cycle of wind intensity (Fig. 11) allowed identifying increases from 0.008 a 0.02 $ms^{-1}year^{-1}$. Increases in wind intensity were predominant in regions of low orography (< 200 m). In July, this increase could be observed in most the region; in the rest of the months, these increases were mainly located in the north and south. In December, the increases occurred in the central region adjacent to the Pacific Ocean.

The analysis of the temporal trends in the time series of dust emission in the three selected zones in the RSBCP (Table 6) for the 1981–1999 and 2001–2020 intervals shows that dust emission has a predominance of positive trends in the Northern region and a predominance of negative trends in the Central and Southern regions. Increases occurred mainly in May, July, October, and November, while decreases occurred in March, April, June, and August.

The trend analysis for desert dust deposition in LPB during 2003–2020, at 95% confidence level before and after the breakpoint (Table 7), allowed establishing an average decrease of $-7 \times 10^{-4} mgm^{-2}day^{-1}year^{-1}$ for the wet deposition mechanism and $-0.01 mgm^{-2}day^{-1}year^{-1}$ for dry deposition.

Table 6 Annual cycle of desert dust emission trends ($mgm^{-2}s^{-1}year^{-1}$) from the three source regions during the period 1981 to 2020, before and after the breakpoint evaluated with the Pettitt test (1979). In addition, trends were evaluated with the Modified Mann–Kendall and Theil-Sen test at 95% significance

Region	Evaluated Time	Jan	Feb	Mar	Apr	May	Jun	Jul	Aug	Sep	Oct	Nov	Dec
North	*Before*	-	-	-	-	-	-	-	-3.83	-	4.44	-	-
	After	-	-	-	-6.92	-	-	3.34	-	-	-	2.50	-
Center	*Before*	-	-	-	-	-	-8.94	-	-	-	-	-	-
	After	-	-	-4.01	-	11.1	-	-	-	-	-	-	-
South	*Before*	-	-	-	-	-	-6.04	-	-	-	-	-	-
	After	-	-	-3.42	-	7.51	-	-	-	-	-	-	-

Table 7 Annual cycle of dry and wet desert dust deposition trends ($mgm^{-2}day^{-1}year^{-1}$) in LPB during 2003 to 2020. Before (2003–2010) and after (2012–2020), the breakpoint was evaluated with the Pettitt test (1979). In addition, trends were evaluated with the Modified Mann–Kendall and Theil-Sen test at 95% confidence level

Deposition	Evaluated Time	Jan	Feb	Mar	Apr	May	Jun	Jul	Aug	Sep	Oct	Nov	Dec
Wet	*Before*	-	-	-	-0.001	-	-0.0001	-	-	-	-	-	-
	After	-	-	-0.001	-	-	-	-	-	-	-	-	-
Dry	*Before*	-	-	-	-	-	-	-	-	-	-	-	-
	After	-	-0.01	-	-0.018	-	-	-	-	-	-0.016	-	-

Discussion

The inverse NLPCA approach applied to the time series with missing data from the CLICOM network allowed us to identify that the extraction of the nonlinear components directly from incomplete data and their subsequent nonlinear mapping reconstructed the time series, maintaining the variability and values of the original series, verifying the above with the comparative metrics proposed by Scholz et al. (2008).

The comparison metrics obtained between CHIRPS-v2.0 data and CLICOM network rain gauges used in this work (Fig. 2) guarantee the validity of the satellite database use, and agree with the values reported in Colombia (Estupiñan-Castellanos 2016; Morales-Acuña et al. 2021), Venezuela (Paredes Trejo et al. 2016), África (Dinku et al. 2018) and Ethiopia (Alemu & Bawoke 2019), who confirms that despite the slight underestimation of CHIRPS-v2.0 this database represents rainfall's variability and its means values. In addition, the comparisons of CLICOM and ERA5-Land (Fig. 3) confirmed that although this database slightly overestimates the values measured in situ, it faithfully represents the magnitude and variability of the time series, agreeing with Cao et al. (2020), Pelosi et al. (2020), Retamales-Muñoz et al. (2019) and Tetzner et al. (2019), who recommend the use of the ERA5-Land database to identify and analyze climate patterns in different regions of the world.

The spatial distribution of rainfall establishes a latitudinal gradient from south to north, due to the pluviometric regime reported by Salinas-Zavala et al. (1990) and Troyo-Diéguez et al. (2014), who explains these differences due geographical differences. The rainfall climatology allowed classify two rainy seasons and one dry season that coincide with that reported by Salinas-Zavala et al. (1990), but the present work determined two transition months: February and October. The rainfall season and maximum rainfall are in the mountain regions located south of the study area. This season coincides with the tropical cyclone season and the significantly increasing linear trends of heavy rainfall in mountain sites reported by Cavazos et al. (2008). This rainfall contributes 40% of the total annual rainfall for the Baja California Peninsula (Breña-Naranjo et al. 2015). The climatology for air temperature found in the present study (Fig. 5) allowed the identification of warm and cold seasons, consisting of the months of summer (June–September) and winter (December-March), congruent with Troyo-Diéguez et al. (2014) and INEGI (2011). In addition, the month of November is proposed as a transition period between maximum and minimum temperatures.

The longitudinal west–east gradient for the wind intensity found in this study (Fig. 7) can be attributed to the influence of northern winds in the eastern coastal region of the study area, as reported by Morales-Acuña et al. (2019a, b) and Castro & Martínez (2010). Also, the predominance in the wind direction during the summer season (Fig. 8) agrees with the west–east direction reported by Morales-Acuña et al. (2019a, b). The redirection and behavior that air masses have when encountering the mountain located south of the region from April to September (Fig. 8) could be attributed to Froude number values < 1 (Nappo 2013), such that, when this condition is met, atmospheric flows tend to go around obstacles found in their trajectory. The predominant southwesterly direction in the RSBCP during the winter months (November-February) responds to the seasonal winter pattern and the displacement of the North Pacific high-pressure center, which in this season is directed towards the equator (Badan-Dangon et al. 1991; Morales-Acuña et al. 2019b; Romero-Centeno et al. 2007).

The analysis and quantification of emission and deposition (Figs. 7 and 8), showed that in the three source regions studied, there is a unimodal behavior in the emission rates where the maximum emissions are during spring–summer and minimum in winter, coinciding with those reported by Morales-Acuña et al. (2019b), for the Vizcaíno desert. If we consider the annual cycle fluctuations of the hydrometeorological variables analyzed, it can be suggested that this behavior of maximum emission rates responds to favorable conditions that facilitate the atmospheric flows of desert dust from each of the regions (North, Central, and South) to the LPB, mainly during March to June, due to the dry season, average temperatures, and winds with predominantly easterly direction.

Regarding deposition, although the wet deposition mechanism plays an essential role in the supply of nutrients and toxic substances to terrestrial and aquatic environments (Pan et al. 2017). In this study, it was determined that the primary mechanism for carrying out desert dust intrusions resulting from emissions and dispersion from the analyzed source areas to the LPB is through dry deposition, being 0.1661 $mgm^{-2}s^{-1}$ higher than wet deposition, this behavior may be due to the climatic characteristics in the RSBCP as a semi-desert area where most of the year the accumulated rainfall is less than 500 $mmmonth^{-1}$ (Fig. 4), and the wind shows optimal conditions of intensity, 75% of the year (Fig. 6), which would favor erosion and subsequent dust deposition. In addition, Zhao et al. (2003) suggest that dry deposition is a dominant dust removal process near the source areas (as is the case of the LPB), and the removal of dust particles by rainfall turns out to be the primary process in the transport pathway in regions distant from the source. Comparing the dust fluxes emitted from each source with the atmospheric depositions in the LPB, we find very marked differences suggesting that not everything emitted from the source regions tends to be deposited in the LPB. This behavior is comparable with the balances of desert dust fluxes obtained from models. In many world regions, dust fluxes are not in balance because the transport models generally do not conserve mass due to the time interpolation techniques that they usually use (Ginoux et al. 2004). Additionally, if we compare the normalized values by area obtained in the present study with the emission and deposition of dust in other regions of the world (Table. 8); it is inferred that: RSBCP and LPB, are not very relevant to the global desert dust budget, but a very significant local contribution for the region, as is the case in Japan and its coasts (Osada et al. 2014).

The analysis of the breaking point in the monthly climatology of time series identified an abrupt change in the year 2000 for the variable's rainfall, air temperature, wind, and dust emission, while for the mechanisms of deposition of airborne dust in the LPB, the change in the series occurred in 2011. By repeating this analysis to the complete series (at 95% confidence level), it was possible to determine that in both cases, the change took place precisely in December of the corresponding year. Taking into account that fluctuations in the time series of atmospheric, hydrological, and oceanographic variables generally depend on atmospheric phenomena such as El Niño Southern Oscillation (ENSO), the Pacific Decadal Oscillation (PDO) (Alvarez-Olguin and Escalante-Sandoval 2017; Arriaga-Ramírez & Cavazos 2010; Llanes-Cárdenas et al. 2018) and solar activity, monthly time series of the indices, Southern Oscillation (SOI, https://www.ncdc.noaa.gov/teleconnections/enso/soi), PDO (https://www.ncdc.noaa.gov/teleconnections/pdo/) and sunspots (Sunspot, https://wwwbis.sidc.be/silso/monthlyssnplot were obtained. These time series were smoothed with the Lanczos cosine filter (Duchon 1979) low pass, with a 12-month window (Fig. 12). It was found that in the periods corresponding to the breakpoints obtained in the present work, the solar activity presents positive anomalies (Fig. 12, insets). In addition, it could be identified that during this period of positive sunspot anomalies, the PDO and SOI present inverse anomalies between 1 and—2 standard deviations (Fig. 12), out of phase -3 months at 95% confidence level.

The progressive decreases in rainfall found in the present study (Fig. 9) suggest a temporal extension of the dry season, thus affecting the pluviometric regime of the region and establishing a unimodal behavior in which

Table 8 Annual emission, deposition dry and wet (Tg yr^{-1}) of mineral dust Emission. Percentage of global estimates is shown in parentheses

References	Emission	Dry Depositon	Wet Deposition	Total Deposition	Region
Chen et al. (2022)	11*			27 (1.43%)	North America
	3*			11*	South America
	1112 (59.24%)			685 (36.5%)	North Africa
Morales-Acuña et al. (2019b)	1.5*				Vizcaíno, México
Osada et al. (2014)		0.01*	0.004*		Toyama, Japan
		0.004*	0.003*		Tottori, Japan
		0.002*	0.001*		Fukuoka, Japan
Hsu et al. (2009)		4.46*	12.01 (1.78%)	16.47*	Southern East China Sea
O'Hara et al. (2006)				4 (0.21%)	Libya: Southern
Uematsu et al. (2003)		44.1 (3.6%)	29.4 (4.35%)	73.5 (3.9%)	Chinese coastal sea
Zhang et al. (1997)				151.7 (8.1%)	Taklimakan Desert
				6.24*	Gurbantunggut Desert
Tanaka & Chiba (2006)	1877	1202	675	1877	Global
This study	0.32*	1.4E-5*	1.65E-7*	1.41E-5*	RSBCP and LPB

* Insignificant percentage values on the global scale (< 1%)

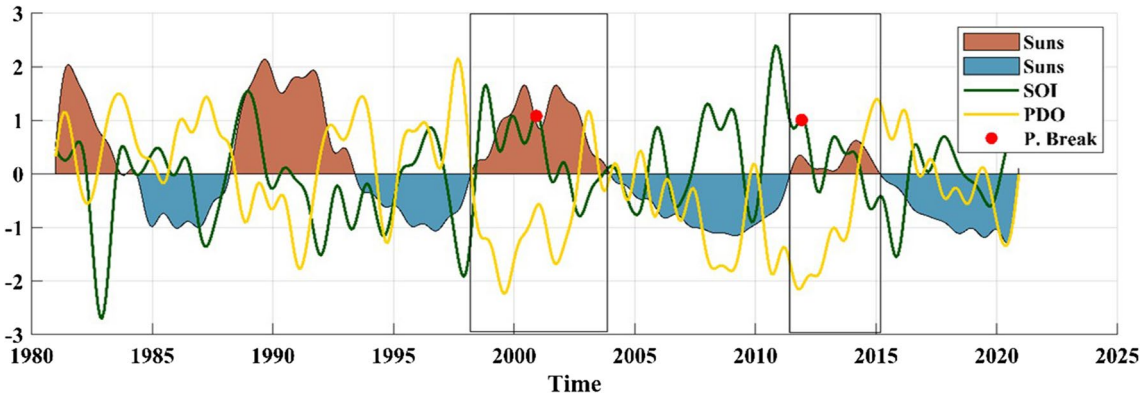

Fig. 12 Time series filtered with Lanczos cosine with a 12-month window for the climate indices: Sunspot (shaded areas in red and blue), SOI in the green line, and PDO in the yellow line. The red dots show the breakpoints (P. Break) obtained in the time series of the variables analyzed in this study. The inset shows the periods of the positive sunspot anomalies contained in the time interval of the breakpoints

there would be a rainy season (June–September) and the rest of the dry season. These decreases are congruent with those reported by Blunden & Arndt (2016) and Morales-Acuña et al. (2019b) for this region of Mexico, even so, in an exercise for the detection of the trend between 1960 and 2010 carried out by Núñez-González (2020), in 6 stations located in the RSBCP determined the existence of no annual trend, negative trends for winter-summer and favorable trends for autumn.

The increases in air temperature (Fig. 10) established during the winter and summer months (which in turn represent the seasons with the most remarkable differences), increases of ~ 0.02 °C that could affect the economic activities of the region, characterized by focusing part of its economy on agricultural activities with cyclical crops during the autumn–winter, spring–summer seasons. In addition, in terms of desert dust emissions, these increases in air temperature would favor fluxes to the atmosphere due to the lack of soil moisture resulting from soil evaporation processes. The temperature increases found in the present study are in agreement with those reported by the IPCC (2019), which estimates that global temperature will increase between 0.1 and 0.3 °C per decade, while seasons in some regions are experiencing warming; in addition, results reported by Blunden & Arndt (2016) and Morales-Acuña et al. (2019b), who reported positive trends for the Vizcaíno region.

The predominance of increasing trends in dust emission for the northern region of the present study is congruent with the increases in this variable in the Vizcaíno desert reported by Morales-Acuña et al. (2019b). Furthermore, the months in which increases in dust emission occurred (May, July, October, and November) coincide with the increasing trends in wind intensity, air temperature, and decreases in rainfall obtained in the present study. In addition, the months with decreasing trends coincide with the predominance of no statistically significant trend for the climatic variables evaluated in the dust source regions. Finally, the decreases in the wet and dry deposition mechanisms obtained in this work are congruent and respond to the decreasing trends in rainfall and increases in wind intensity, which regulate these mechanisms.

Finally, considering that the direct and indirect radiative effects of terrigenous particles affect climate from regional to global scales (Myhre et al. 2014), specifically "direct effect" by absorbing and scattering solar radiation, desert dust particles reduce the amount of energy reaching the Earth's surface while enhancing the greenhouse effect by absorbing and emitting longwave radiation (Spyrou 2018). The intensification of rainfall in the southern mountainous region found in the present study from July to September (Fig. 4) could be related not only to the presence of tropical cyclones, which in turn have reduced their activity in the North Atlantic due to factors such as dust intrusion from the Sahara (Strong et al. 2018), but also the change in radiative forcing and its impact on local climate parameters such as precipitation and air temperature (Liu et al. 2014; Rap et al. 2013). Specifically for precipitation, studies have shown that desert dust inputs can affect regional water resources by modulating rainfall distribution (Jha et al. 2021), such that these dust inputs sometimes enhance heavy rainfall events and suppress light rainfall events (Alizadeh-Choobari 2018; Li et al. 2011). Consistent with the negative trends in precipitation found in the present work, strong atmospheric inputs of desert dust in turn reduce precipitation by drying out the soil and producing more dust, providing a possible feedback loop to further reduce precipitation (Rosenfeld et al. 2001). On the other hand, the positive air temperature trends obtained in the present work (Fig. 5) could be related to the reduction of incoming solar radiation at the surface (Slingo et al. 2006), he increase in daily heating rates

(Chen et al. 2017) and the warming of the middle troposphere and cooling of the lower troposphere (Mohalfi et al. 1998), resulting from atmospheric intrusions of desert dust. In addition, the sixth leading cause of mortality in the state of Baja California Sur is acute respiratory infections, with a rate of 1.9 predicted by the Ministry of Health in 2018 for 2050, and it is expected that one of the possible causes of this public health problem is the inhalation of dust particles with diameters less than or equal to 10 microns, as has been reported in southern Europe (Stafoggia et al. 2016), Madrid (Diaz-Jiménez et al. 2012), Cuba (Venero-Fernández 2016), among others. Also for larger sizes of dust particles, it has been found that they can potentially damage external organs, irritating eyes and ears (Zhang et al. 2016). This raises the alarm in the study region for the development of studies and action plans focused on the effects of atmospheric dust intrusion on public health.

Conclusions

The time series reconstruction techniques applied to the CLICOM database and validation of the reanalysis and remote sensing products used in this work showed statistically significant metrics that guaranteed the use of the data obtained for the study region after the pre-processing to which they were subjected.

Although the analysis of climate in the RSBCP (1981–2020) temporally and spatially classifies rainfall, air temperature, and wind within the annual cycle, trend analyses determine that this classification is affected by increases in air temperature and wind intensity and decreases in rainfall. It causes the wind (predominant direction is towards the east and southeast) to transport moisture away from the peninsular region, and in turn, it generates more extended droughts, warmer winters, and hotter summers.

Since the emission of desert dust is driven mainly by the wind intensity and rainfall, the primary mechanism of deposition of this terrigenous material on the LPB is dry deposition. It is deduced that the fluctuations and trends of the hydrometeorological variables affect the production of desert dust, thus finding a predominance of positive trends in the region of lower rainfall (North) and negative trends in the opposite case (South). In the months where decreasing trends in rainfall, increases in air temperature, and wind intensity converge, dust emissions from the different zones were increasing. However, dust deposition over the LPB has a decreasing trend because it is controlled mainly by fluctuations in wind intensity, so it is suggested that due to increases in wind intensity and the predominance in the direction towards the east and southeast, most of the dust emitted from the peninsula is deposited in the southern Gulf of California.

Finally, the found convergence between the representative indexes (solar activity, the PDO and the SOI, the last two out of phase by -3 months), and the temporal breakpoints (different time series analyzed) represents particular interest to carry out studies on the implications of climate indexes on the trends and temporal fluctuations of hydrometeorological and environmental variables.

Acknowledgements The authors would like to thank the project "Ciencia de Frontera" CONACyT N° 6364 entitled *"La producción exportada y los flujos biogeoquímicos verticales en un escenario de incremento en la temperatura y acidificación del mar"* for the financial support for this research. To the Faculty of Engineering Sciences of the Universidad del Magdalena, the computer equipment for downloading and processing the data. Morales-Acuña thanks the program "Estancias Postdoctorales por México" called 2021, modality by incidence, for the economic support during the stay at the Interdisciplinary Center of Marine Sciences of the IPN.

Author's contribution Morales-Acuña, contributed with the processing, analysis and interpretation of the data and writing of the document. Aguíñiga-Garcia, contributed with the analysis of results and revision of the manuscript. Cervantes-Duarte, contributed with the revision of the manuscript. Finally, Linero-Cueto, contributed with the writing of the manuscript, analysis, and interpretation of the results.

Funding Open Access funding provided by Colombia Consortium Open Access funding provided by Colombia Consortium.

Availability of data and materials Contact the corresponding author.

Declarations

Competing interests The authors declare no competing interests.

Conflict of interest The authors declare that there is no conflict of interest.

References

Alemu, M. M., & Bawoke, G. T. (2020). Analysis of spatial variability and temporal trends of rainfall in Amhara region, Ethiopia. Journal of Water and Climate Change, 11(4):1505–1520

Aliaga VS, Ferrelli F, Piccolo MC (2017) Regionalization of climate over the Argentine Pampas. Int J Climatol 37(S1):1237–1247. https://doi.org/10.1002/joc.5079

Alizadeh-Choobari O (2018) Impact of aerosol number concentration on precipitation under different precipitation rates. Meteorol Appl 25(4):596–605. https://doi.org/10.1002/met.1724

Almazroui M, Saeed F, Saeed S, Nazrul Islam M, Ismail M, Klutse NAB, Siddiqui MH (2020) Projected Change in Temperature and Precipitation Over Africa from CMIP6. Earth Syst Environ 4(3):455–475. https://doi.org/10.1007/s41748-020-00161-x

Alvarez-Olguin G, Escalante-Sandoval C (2017) Modes of Variability of Annual and Seasonal Rainfall in Mexico. JAWRA J Am Water Resour Assoc 53(1):144–157. https://doi.org/10.1111/1752-1688.12488

Arriaga-Ramírez S, Cavazos T (2010) Regional trends of daily precipitation indices in northwest Mexico and southwest United States. J Geophys Res Atmos 115(D14). https://doi.org/10.1029/2009JD013248

Badan-Dangon A, Dorman CE, Merrifield MA, Winant CD (1991) The lower atmosphere over the Gulf of California. J Geophys Res Oceans 96(C9):16877–16896. https://doi.org/10.1029/91JC01433

Bergametti G, Forêt G (2014) Dust Deposition. In: Knippertz P, Stuut J-BW (Eds.), Mineral Dust: A Key Player in the Earth System. Springer, Netherlands, pp. 179–200. https://doi.org/10.1007/978-94-017-8978-3_8

Blunden J, Arndt DS (2016) State of the Climate in 2015. Bull Am Meteorol Soc 97(8):Si-S275. https://doi.org/10.1175/2016BAMSStateoftheClimate.1

Breña-Naranjo AJ, Pedrozo-Acuña A, Pozos-Estrada O, Jiménez-López SA, López-López MR (2015) The contribution of tropical cyclones to rainfall in Mexico Physics and Chemistry of the Earth. Parts a/b/c 83–84(111):122. https://doi.org/10.1016/j.pce.2015.05.011

Canchala T, Alfonso-Morales W, Carvajal-Escobar Y, Cerón WL, Caicedo-Bravo E (2020) Monthly Rainfall Anomalies Forecasting for Southwestern Colombia Using Artificial Neural Networks Approaches. Water 12(9):9. https://doi.org/10.3390/w12092628

Cao B, Gruber S, Zheng D, Li X (2020) The ERA5-Land soil temperature bias in permafrost regions. Cryosphere 14(8):2581–2595. https://doi.org/10.5194/tc-14-2581-2020

Castro Valdez R, Martínez J (2010) Variabilidad espacial y temporal del campo de viento frente a la Península de Baja California, pp 129–147

Cavazos T, Turrent C, Lettenmaier DP (2008) Extreme precipitation trends associated with tropical cyclones in the core of the North American monsoon. Geophys Res Lett 35(21). https://doi.org/10.1029/2008GL035832

Chen D, Liu Z, Davis C, Gu Y (2017) Dust radiative effects on atmospheric thermodynamics and tropical cyclogenesis over the Atlantic Ocean using WRF-Chem coupled with an AOD data assimilation system. Atmos Chem Phys 17(12):7917–7939. https://doi.org/10.5194/acp-17-7917-2017

Chen W, Meng H, Song H, Zheng H (2022) Progress in Dust Modelling, Global Dust Budgets, and Soil Organic Carbon Dynamics. Land 11(2):2. https://doi.org/10.3390/land11020176

Colorado-Ruiz G, Cavazos T (2021) Trends of daily extreme and non-extreme rainfall indices and intercomparison with different gridded data sets over Mexico and the southern United States. Int J Climatol 41(11):5406–5430. https://doi.org/10.1002/joc.7225

de Barros DS, Lee H, Loikith PC, Barkhordarian A, Mechoso CR (2016) Can significant trends be detected in surface air temperature and precipitation over South America in recent decades? Int J Climatol 37(3):1483–1493. https://doi.org/10.1002/joc.4792

Diaz-Jimenez J, Tobías A, Linares-Gil C (2012) Saharan dust and association between particulate matter and case-specific mortality: A case-crossover analysis in Madrid (Spain). Environ Health 11:11. https://doi.org/10.1186/1476-069X-11-11

Dinku T, Funk C, Peterson P, Maidment R, Tadesse T, Gadain H, Ceccato P (2018) Validation of the CHIRPS satellite rainfall estimates over eastern Africa. Q J R Meteorol Soc 144(S1):292–312. https://doi.org/10.1002/qj.3244

Duchon CE (1979) Lanczos Filtering in One and Two Dimensions. J Appl Meteorol Climatol 18(8):1016–1022. https://doi.org/10.1175/1520-0450(1979)018%3c1016:LFIOAT%3e2.0.CO;2

Estupiñan-Castellanos AR (2016) *Estudio de la variabilidad espacio temporal de la precipitación en Colombia* [Masters, Universidad Nacional de Colombia – Sede Medellín]. http://www.bdigital.unal.edu.co/54014/

Evan AT, Vimont DJ, Heidinger AK, Kossin JP, Bennartz R (2009) The Role of Aerosols in the Evolution of Tropical North Atlantic Ocean Temperature Anomalies. Science 324(5928):778–781. https://doi.org/10.1126/science.1167404

Funk C, Peterson P, Landsfeld M, Pedreros D, Verdin J, Shukla S, Husak G, Rowland J, Harrison L, Hoell A, Michaelsen J (2015) The climate hazards infrared precipitation with stations—A new environmental record for monitoring extremes. Scientific Data 2(1):150066. https://doi.org/10.1038/sdata.2015.66

Ginoux P (2017) Warming or cooling dust? Nature Geoscience 10(4):4. https://doi.org/10.1038/ngeo2923

Ginoux P, Prospero JM, Torres O, Chin M (2004) Long-term simulation of global dust distribution with the GOCART model: Correlation with North Atlantic Oscillation. Environ Model Softw 19(2):113–128. https://doi.org/10.1016/S1364-8152(03)00114-2

Ginoux P, Prospero JM, Gill TE, Hsu NC, Zhao M (2012) Global-scale attribution of anthropogenic and natural dust sources and their emission rates based on MODIS Deep Blue aerosol products. Rev Geophys 50(3). https://doi.org/10.1029/2012RG000388

Hamed KH, Rao A (1998) A modified Mann-Kendall trend test for autocorrelated data. J Hydrol 204(1):182–196. https://doi.org/10.1016/S0022-1694(97)00125-X

Hsu S-C, Liu SC, Arimoto R, Liu T-H, Huang Y-T, Tsai F, Lin F-J, Kao S-J (2009) Dust deposition to the East China Sea and its biogeochemical implications. J Geophys Res Atmos 114(D15). https://doi.org/10.1029/2008JD011223

INEGI (2010) *Compendio de información geográfica municipal 2010. La Paz, Baja California Sur.* Instituto Nacional de Estadística y Geografía. https://www.inegi.org.mx/contenidos/app/mexicocifras/datos_geograficos/03/03003.pdf

INEGI (2011) *Baja California Sur: Panorama sociodemográfico*. 27

IPCC. (2014) Climate Change 2013: The Physical Science Basis: Working Group I Contribution to the Fifth Assessment Report of the Intergovernmental Panel on Climate Change. Cambridge University Press.

IPCC. (2015) Climate Change 2014: Synthesis Report. Contribution of Working Groups I, II and III to the Fifth Assessment Report of the Intergovernmental Panel on Climate Change. En EPIC3Geneva, Switzerland, IPCC, 151 p., pp. 151, ISBN: 978–92–9169–143–2 (p. 151). IPCC. https://epic.awi.de/id/eprint/37530/

IPCC. (2019) *Calentamiento global de 1,5 °C: Informe especial del IPCC sobre los impactos del calentamiento global de 1,5 °C con respecto a los niveles preindustriales y las trayectorias correspondientes que deberían seguir las emisiones mundiales de gases de efecto invernadero, en el contexto del reforzamiento de la respuesta mundial a la amenaza del cambio climático, el desarrollo sostenible y los esfuerzos por erradicar la pobreza*. Intergovernmental Panel on Climate Change. https://www.ipcc.ch/site/assets/uploads/sites/2/2019/09/IPCC-Special-Report-1.5-SPM_es.pdf

Jardim AMDARF, da Silva MV, da Silva AR, dos Santos A, Pandorfi H, de Oliveira-Júnior JF, de Lima JLMP, de Souza LSB, Araújo Júnior GdoN, Lopes PMO, Moura GBdeA, Silva TGF (2021) Spatiotemporal climatic analysis in Pernambuco State, Northeast Brazil. J Atmos Sol Terr Phys 223:105733. https://doi.org/10.1016/j.jastp.2021.105733

Jha V, Cotton WR, Carrió GG, Walko R (2021) Seasonal estimates of the impacts of aerosol and dust pollution on orographic precipitation in the Colorado River Basin. Phys Geogr 42(1):73–97. https://doi.org/10.1080/02723646.2020.1792602

Ji Z, Wang G, Yu M, Pal JS (2018) Potential climate effect of mineral aerosols over West Africa: Part II—contribution of dust and land cover to future climate change. Clim Dyn 50(7):2335–2353. https://doi.org/10.1007/s00382-015-2792-x

Kok JF, Storelvmo T, Karydis V, Adebiyi AA, Mahowald NM, Evan AT, He C, Leung D (2022) Mineral dust aerosol impacts on global climate and climate change. https://eartharxiv.org/repository/view/3577/

Li Z, Niu F, Fan J, Liu Y, Rosenfeld D, Ding Y (2011) Long-term impacts of aerosols on the vertical development of clouds and precipitation. Nat Geosci 4(12):12. https://doi.org/10.1038/ngeo1313

Liu Y, Jia R, Dai T, Xie Y, Shi G (2014) A review of aerosol optical properties and radiative effects. J Meteorol Res 28(6):1003–1028. https://doi.org/10.1007/s13351-014-4045-z

Llanes-Cárdenas O, Gaxiola-Hernández A, Estrella-Gastelum RD, Norzagaray-Campos M, Troyo-Diéguez E, Pérez-González E, Ruiz-Guerrero R, Pellegrini De J, Cervantes M (2018) Variability and Factors of Influence of Extreme Wet and Dry Events in Northern Mexico. Atmosphere 9(4):4. https://doi.org/10.3390/atmos9040122

Mahowald N, Albani S, Kok JF, Engelstaeder S, Scanza R, Ward DS, Flanner MG (2014) The size distribution of desert dust aerosols and its impact on the Earth system. Aeol Res 15:53–71. https://doi.org/10.1016/j.aeolia.2013.09.002

Martinez Avellaneda N (2010) *The Impact of Saharan Dust on the North Atlantic Circulation* [DoctoralThesis, Staats- und Universitätsbibliothek Hamburg Carl von Ossietzky]. https://ediss.sub.uni-hamburg.de/handle/ediss/3629

Martínez-Austria PF, Jano-Pérez JA (2021) Climate Change and Extreme Temperature Trends in the Baja California Peninsula, Mexico. Air, Soil Water Res 14:11786221211010702. https://doi.org/10.1177/11786221211010702

Martínez-Flores G, Segovia-Zavala JA, García-Álvarez Y (2013) Variabilidad espacio-temporal de la circulación atmosférica en el Noroeste de México. In: XX congreso nacional de ciencia y tecnología del mar (Vol. 1, p. 16)

Miró JJ, Caselles V, Estrela MJ (2017) Multiple imputation of rainfall missing data in the Iberian Mediterranean context. Atmos Res 197:313–330. https://doi.org/10.1016/j.atmosres.2017.07.016

Mohalfi S, Bedi HS, Krishnamurti TN, Cocke SD (1998) Impact of Shortwave Radiative Effects of Dust Aerosols on the Summer Season Heat Low over Saudi Arabia. Mon Weather Rev 126(12):3153–3168. https://doi.org/10.1175/1520-0493(1998)126%3c3153:IOSREO%3e2.0.CO;2

Morales-Acuña E, Torres CR, Delgadillo-Hinojosa F, Linero-Cueto JR, Santamaría-del-Ángel E, Castro R (2019a) The Baja California Peninsula, a Significant Source of Dust in Northwest Mexico. Atmosphere 10(10):582. https://doi.org/10.3390/atmos10100582

Morales-Acuña E, Torres CR, Linero-Cueto JR (2019b) Surface wind characteristics over Baja California Peninsula during summer. Regional Studies in Marine Science 29:100654. https://doi.org/10.1016/j.rsma.2019.100654

Morales-Acuña E, Linero-Cueto JR, Canales FA (2021) Assessment of Precipitation Variability and Trends Based on Satellite Estimations for a Heterogeneous Colombian Region. Hydrology 8(3):3. https://doi.org/10.3390/hydrology8030128

Muñoz-Barbosa A, Delgadillo-Hinojosa F, Torres-Delgado EV, Félix-Bermúdez A, Castro R (2020) Bajacalifornian dust deposition and atmospheric input of iron to the Gulf of California during the summer. Marine Chemistry 225:103850. https://doi.org/10.1016/j.marchem.2020.103850

Myhre G, Shindell D, Pongratz J, Stocker T (2014) *Anthropogenic and Natural Radiative Forcing* (T. Stocker, Ed.; pp. 659–740). Ludwig-Maximilians-Universität München. https://doi.org/10.1017/CBO9781107415324.018

Nappo CJ (2013) An introduction to atmospheric gravity waves (2nd ed), Academic Press

Nazarian RH, Vizzard JV, Agostino CP, Lutsko NJ (2022) Projected Changes in Future Extreme Precipitation over the Northeast United States in the NA-CORDEX Ensemble. J Appl Meteorol Climatol 61(11):1649–1668. https://doi.org/10.1175/JAMC-D-22-0008.1

Nickling WG, Gillies JA (1993) Dust emission and transport in Mali. West Africa Sedimentol 40(5):859–868. https://doi.org/10.1111/j.1365-3091.1993.tb01365.x

Nickovic S, Kallos G, Papadopoulos A, Kakaliagou O (2001) A model for prediction of desert dust cycle in the atmosphere. J Geophys Res Atmos 106(D16):18113–18129. https://doi.org/10.1029/2000JD900794

Núñez-González G (2020) Analysis of the trends in precipitation and precipitation concentration in some climatological stations of Mexico from 1960 to 2010. Nat Hazards 104(2):1747–1761. https://doi.org/10.1007/s11069-020-04244-w

O'Hara SL, Clarke ML, Elatrash MS (2006) Field measurements of desert dust deposition in Libya. Atmos Environ 40(21):3881–3897. https://doi.org/10.1016/j.atmosenv.2006.02.020

Okin GS, Reheis MC (2002) An ENSO predictor of dust emission in the southwestern United States. Geophys Res Lett 29(9):46-1–46-3. https://doi.org/10.1029/2001GL014494

Osada K, Ura S, Kagawa M, Mikami M, Tanaka TY, Matoba S, Aoki K, Shinoda M, Kurosaki Y, Hayashi M, Shimizu A, Uematsu M (2014) Wet and dry deposition of mineral dust particles in Japan: Factors related to temporal variation and spatial distribution. Atmos Chem Phys 14(2):1107–1121. https://doi.org/10.5194/acp-14-1107-2014

Pan Y-P, Zhu X-Y, Tian S-L, Wang L-L, Zhang G-Z, Zhou Y-B, Xu P, Hu B, Wang Y-S (2017) Wet deposition and scavenging ratio of air pollutants during an extreme rainstorm in the North China Plain. Atmos Ocean Sci Lett 10(5):348–353. https://doi.org/10.1080/16742834.2017.1343084

Paredes Trejo FJ, Barbosa HA, Peñaloza-Murillo MA, Alejandra Moreno M, Farías A (2016) Intercomparison of improved satellite rainfall estimation with CHIRPS gridded product and rain gauge data over Venezuela. Atmósfera 29(4):323–342. https://doi.org/10.20937/ATM.2016.29.04.04

Peinado M, Aguirre JL, Delgadillo J, Macías MÁ (2008) A phytosociological and phytogeographical survey of the coastal vegetation of western North America. Part I: Plant communities of Baja California Mexico. Plant Ecol 196(1):27–60. https://doi.org/10.1007/s11258-007-9334-5

Pelosi A, Terribile F, D'Urso G, Chirico GB (2020) Comparison of ERA5-Land and UERRA MESCAN-SURFEX Reanalysis Data with Spatially Interpolated Weather Observations for the Regional Assessment of Reference Evapotranspiration. Water 12(6):6. https://doi.org/10.3390/w12061669

Pettitt AN (1979) A Non-Parametric Approach to the Change-Point Problem. J Roy Stat Soc: Ser C (appl Stat) 28(2):126–135. https://doi.org/10.2307/2346729

Pu B, Ginoux P (2017) Projection of American dustiness in the late 21st century due to climate change. Sci Rep 7(1):1. https://doi.org/10.1038/s41598-017-05431-9

Rap A, Scott CE, Spracklen DV, Bellouin N, Forster PM, Carslaw KS, Schmidt A, Mann G (2013) Natural aerosol direct and indirect radiative effects. Geophys Res Lett 40(12):3297–3301. https://doi.org/10.1002/grl.50441

Retamales-Muñoz G, Durán-Alarcón C, Mattar C (2019) Recent land surface temperature patterns in Antarctica using satellite and

reanalysis data. J South Am Earth Sci 95:102304. https://doi.org/10.1016/j.jsames.2019.102304

Romero-Centeno R, Zavala-Hidalgo J, Raga GB (2007) Midsummer Gap Winds and Low-Level Circulation over the Eastern Tropical Pacific. J Clim 20(15):3768–3784. https://doi.org/10.1175/JCLI4220.1

Rosenfeld D, Rudich Y, Lahav R (2001) Desert dust suppressing precipitation: A possible desertification feedback loop. Proc Natl Acad Sci 98(11):5975–5980. https://doi.org/10.1073/pnas.101122798

S.M.N. (2023) *Base climatológica diaria. Servicio Meteorológico Nacional*. Comisión Nacional del Agua. Normales Climatológicas por Estación. México. https://smn.conagua.gob.mx/es/

Safaierad R, Mohtadi M, Zolitschka B, Yokoyama Y, Vogt C, Schefuß E (2020) Elevated dust depositions in West Asia linked to ocean–atmosphere shifts during North Atlantic cold events. Proc Natl Acad Sci 117(31):18272–18277. https://doi.org/10.1073/pnas.2004071117

Salinas-Zavala CA, Martínez-Rincón RO, Morales-Zárate MV (2017) Trend in the Normalized Difference Vegetation Index (NDVI) in the Southern Part of Baja California Peninsula. Investig Geogr 94:9. https://doi.org/10.14350/rig.57214

Salinas-Zavala CA, Contreras AL, Belda DL, Rivera ED (1990) Distribución geográfica y variabilidad climática de los regímenes pluviométricos en Baja California Sur, México. Atmósfera 3(3):3. https://www.revistascca.unam.mx/atm/index.php/atm/article/view/8297

Scholz M, Fraunholz M, Selbig J (2008) Nonlinear Principal Component Analysis: Neural Network Models and Applications. In: Gorban AN, Kégl B, Wunsch DC, Zinovyev AY (Eds.), Principal Manifolds for Data Visualization and Dimension Reduction. Springer. pp. 44–67. https://doi.org/10.1007/978-3-540-73750-6_2

SEMARNAT (2016) *Informe de la Situación del Medio Ambiente en México. Compendio de Estadísticas Ambientales. Indicadores Clave, de Desempeño Ambiental y de Crecimiento Verde*. https://apps1.semarnat.gob.mx:8443/dgeia/informe15/tema/pdf/Informe15_completo.pdf

Sen P (1968) Estimates of the Regression Coefficient Based on Kendall's Tau. J Am Stat Assoc 63(324):1379–1389. https://doi.org/10.1080/01621459.1968.10480934

Shao Y, Raupach MR, Findlater PA (1993) Effect of saltation bombardment on the entrainment of dust by wind. J Geophys Res Atmos 98(D7):12719–12726. https://doi.org/10.1029/93JD00396

Shao Y, Wyrwoll K-H, Chappell A, Huang J, Lin Z, McTainsh GH, Mikami M, Tanaka TY, Wang X, Yoon S (2011) Dust cycle: An emerging core theme in Earth system science. Aeol Res 2(4):181–204. https://doi.org/10.1016/j.aeolia.2011.02.001

Slingo A, Ackerman TP, Allan RP, Kassianov EI, McFarlane SA, Robinson GJ, Barnard JC, Miller MA, Harries JE, Russell JE, Dewitte S (2006) Observations of the impact of a major Saharan dust storm on the atmospheric radiation balance. Geophys Res Lett 33(24):L24817. https://doi.org/10.1029/2006GL027869

Spyrou C (2018) Direct radiative impacts of desert dust on atmospheric water content. Aerosol Sci Technol 52(6):693–701. https://doi.org/10.1080/02786826.2018.1449940

Stafoggia M, Zauli-Sajani S, Pey J, Samoli E, Alessandrini E, Basagaña X, Cernigliaro A, Chiusolo M, Demaria M, Díaz J, Faustini A, Katsouyanni K, Kelessis AG, Linares C, Marchesi S, Medina S, Pandolfi P, Pérez N, Querol X., …null, nullDesert Dust Outbreaks in Southern Europe: Contribution to Daily PM10 Concentrations and Short-Term Associations with Mortality and Hospital Admissions. Environ Health Perspect 124(4):413-419https://doi.org/10.1289/ehp.1409164

Strong JDO, Vecchi GA, Ginoux P (2018) The Climatological Effect of Saharan Dust on Global Tropical Cyclones in a Fully Coupled GCM. J Geophys Res Atmos 123(10):5538–5559. https://doi.org/10.1029/2017JD027808

Tanaka TY, Chiba M (2006) A numerical study of the contributions of dust source regions to the global dust budget. Global Planet Change 52(1):88–104. https://doi.org/10.1016/j.gloplacha.2006.02.002

Tetzner D, Thomas E, Allen C (2019) A Validation of ERA5 Reanalysis Data in the Southern Antarctic Peninsula—Ellsworth Land Region, and Its Implications for Ice Core Studies. Geosciences 9(7):7. https://doi.org/10.3390/geosciences9070289

Troyo-Diéguez E, Mercado Mancera G, Cruz Falcón A, Nieto Garibay A, Valdez Cepeda RD, García Hernández JL, Murillo Amador B (2014) Análisis de la sequía y desertificación mediante índices de aridez y estimación de la brecha hídrica en Baja California Sur, noroeste de México. Investig Geogr 85:66–81. https://doi.org/10.14350/rig.32404

Uematsu M, Wang Z, Uno I (2003) Atmospheric input of mineral dust to the western North Pacific region based on direct measurements and a regional chemical transport model. Geophys Res Lett 30(6). https://doi.org/10.1029/2002GL016645

Urrea V, Ochoa A, Mesa O (2016) Validación de la base de datos de precipitación CHIRPS para Colombia a escala diaria, mensual y anual en el periodo 1981–2014. *XXVII Congreso Latinoamericano de Hidráulica, IAHS, Lima, Perú, URL* http://ladhi2016.org *https://www.researchgate.net/publication/310844678_Validacion_de_la_base_de_datos_de_precipitacion_CHIRPS_para_Colombia_a_escala_diaria_mensual_y_anual_en_el_periodo_1981-2014*

Venero-Fernández SJ (2016) Saharan Dust Effects on Human Health: A Challenge for Cuba's Researchers. MEDICC Rev 18:32–34. https://doi.org/10.1590/MEDICC.2016.18300011

Wang F, Zhao X, Gerlein-Safdi C, Mu Y, Wang D, Lu Q (2017) Global sources, emissions, transport and deposition of dust and sand and their effects on the climate and environment: A review. Front Environ Sci Eng 11(1):13. https://doi.org/10.1007/s11783-017-0904-z

Westphal DL, Toon OB, Carlson TN (1987) A two-dimensional numerical investigation of the dynamics and microphysics of Saharan dust storms. J Geophys Res Atmos 92(D3):3027–3049. https://doi.org/10.1029/JD092iD03p03027

Zhang XY, Arimoto R, An ZS (1997) Dust emission from Chinese desert sources linked to variations in atmospheric circulation. J Geophys Res Atmos 102(D23):28041–28047. https://doi.org/10.1029/97JD02300

Zhang X, Zhao L, Tong DQ, Wu G, Dan M, Teng B (2016) A Systematic Review of Global Desert Dust and Associated Human Health Effects. Atmosphere 7(12):12. https://doi.org/10.3390/atmos7120158

Zhao TL, Gong SL, Zhang XY, McKendry IG (2003) Modeled size-segregated wet and dry deposition budgets of soil dust aerosol during ACE-Asia 2001: Implications for trans-Pacific transport. J Geophys Re Atmos 108(D23):8665–8674. https://doi.org/10.1029/2002JD003363